Phase-sensitive distributed Rayleigh fiber sensing enabling the real-time monitoring of the refractive index with a sub-cm resolution by all-optical coherent pulse compression

Louis Alliot de Borggraef, Hugues Guillet de Chatellus

Research Article Vol. 31, No. 2 / 16 Jan 2023 / Optics Express 1167
Optics EXPRESS

Phase-sensitive distributed Rayleigh fiber sensing enabling the real-time monitoring of the refractive index with a sub-cm resolution by all-optical coherent pulse compression

LOUIS ALLIOT DE BORGGRAEF[1,2] AND HUGUES GUILLET DE CHATELLUS[1,2,*]

[1]Laboratoire Interdisciplinaire de Physique, UGA/CNRS, 38000 Grenoble, France
[2]Univ Rennes, CNRS, Institut FOTON - UMR 6082, 35000 Rennes, France
[*]hugues.guilletdechatellus@univ-rennes1.fr

Abstract: We have developed a novel architecture enabling distributed acoustic sensing in a commercial single-mode fiber with a sub-cm spatial resolution and an interrogation rate of 20 kHz. More precisely, we report the capability of real-time and space-resolved monitoring of the distributed phase and of the refractive index variations along the sensing fiber. The system reported here is optimal in many aspects. While the use of broadband light waveforms enables a sub-cm spatial resolution, the waveforms are quasi CW, delaying the occurrence of non-linear effects. Coherent detection ensures direct access to the distributed phase and to the local variations of the refractive index. Moreover, an all-optical pulse compression feature enables to lower the detection bandwidth down to 10 MSa/s. Based on a bi-directional frequency shifting loop, the architecture makes use of a single CW laser, commercial telecom components, and low frequency electronics. It is expected to open new avenues in distributed acoustic sensing applications, where high spatial resolution and high interrogation rates are required.

1. Introduction

Among numerous remote sensing techniques developed so far, fiber sensors have shown a number of specific advantages, which make them essential in a large number of applications. The latter include remote monitoring of dams, bridges, buildings, railways and sensitive sites, among others [1–4]. Fiber sensors can be placed at specific locations (e.g. Bragg gratings), or distributed along the fiber, which allows interrogation of the sensor continuously, over its entire length [5]. Among the scattering processes implemented in distributed sensors, Rayleigh scattering is particularly attractive since it generally requires less optical power than other scattering processes (Raman and Brillouin). Moreover, it is also sensitive to the phase changes along the fiber [6].

So far, two main interrogation techniques utilizing Rayleigh scattering have been developed. Optical Time Domain Ranging (OTDR) is based on the measurement of the round-trip time of a light pulse from the laser source to the scatterer. The measurement can be based on direct [7], or on coherent detection, where the backscattered signal is mixed with a fraction of the laser [8–10]. Coherent detection offers both longer range and the capability of phase sensitive measurements. The range resolution is directly set by the pulse duration and can be improved by using shorter pulses. As a consequence, the resolution in conventional OTDR is limited by the appearance of non-linear effects triggered by the propagation of short pulses in the fiber, and by the necessity of a high-bandwidth detection chain. Thus, in practice, OTDR is generally used for long distance interrogation with a moderate resolution (meter scale), but it is not adapted to the monitoring of mm or cm scale phenomena. On the contrary, Optical Frequency Domain Ranging (OFDR) potentially offers a spatial resolution down to the cm scale. OFDR makes use of long waveforms with a linear frequency modulation, or chirps [11–13]. The position of the

#479006 https://doi.org/10.1364/OE.479006
Journal © 2023 Received 24 Oct 2022; revised 8 Dec 2022; accepted 9 Dec 2022; published 3 Jan 2023

Optics EXPRESS

scatterer along the fiber is proportional to the frequency of the beatnote between the transmitted and the backscattered waveforms. The resolution is set by the bandwidth of the transmitted chirp. However, OFDR is limited by the requirement of a highly linear chirp and of a fast detection chain. Moreover, the frequency scan of the laser is generally slow, which limits its measurement rate to a few Hz or hundreds of Hz. Therefore, the simultaneous need for high resolution (< cm) and fast interrogation (> kHz) is currently not fulfilled by the available technology.

In this article, we propose a novel architecture of fiber sensor, offering simultaneously a sub-cm resolution, a 20 kHz interrogation rate, and coherent detection. Our approach shows some similarity with phase-sensitive coherent OTDR, where the backscattered waveform is recombined with a reference laser [8–10]. But contrary to OTDR where the resolution is set by the pulse duration, entailing the afore-mentioned drawbacks, we implement a pulse compression operation, which enables us to retrieve a resolution set by the bandwidth of the optical waveforms, and to make use of longer optical waveforms [14]. In practice, pulse compression is achieved by computing the cross-correlation function of the probe waveform with a reference one. Another advantage of pulse compression is the optimization of the signal to noise ratio (SNR) in the case of additive Gaussian noise [15]. The use of pulse compression in fiber sensing has been reported with a modest signal bandwidth (50 MHz), and the need for a fast detection chain (500 MSa/s) [16]. Here, to avoid the use of fast detection and to limit the computing resources required by the signal processing, the pulse compression is not performed digitally, but on an analog fashion. More precisely, an optical reference waveform is generated by the system, so as to enable simultaneously coherent detection, and all-optical analog pulse compression. In terms of performance, our technique is sensitive enough to monitor in real-time the Rayleigh back-scattering signal in a commercial polarization-maintaining single mode fiber with a sub-cm spatial resolution. On a practical point of view, the architecture is strikingly simple. It is based on a bidirectional frequency shifting loop (or FSL), a system made of commercial components at the telecom wavelength. No broadband laser source is needed, but a continuous single-frequency laser. Additionally, no fast electronics is required, and the detection bandwidth does not exceed 5 MHz. We demonstrate direct and quantitative measurement of the distributed phase and of the refractive index variations along the fiber with a spatial resolution of 7 mm, an interrogation rate of 20 kHz and an ambiguity range close to 1 m, which renders the architecture particularly well-suited for the detection and monitoring of fast (< 1 ms) phenomena at the cm scale.

2. Principle of the experiment

2.1. Puse compression in frequency shifting loops (FSLs)

Frequency shifting loops (FSL) have been extensively studied over the last 10 years, especially for applications in microwave-photonics [17–21]. FSLs generate broadband (> 10 GHz) waveforms in a simple architecture, exploiting the recirculation of a single-frequency laser in a loop containing an acousto-optic frequency shifter [22]. The FSL also contains an amplifier to compensate for the losses, and a tunable bandpass filter, to control the spectral bandwidth, and to limit the amplified spontaneous emission (ASE). Depending on the parameters of the FSL, the temporal envelope of the output waveforms can readily be adjusted, from transform-limited pulses, to quasi CW broadband chirped waveforms [23,24]. Recently, FSLs have shown their capability for remote sensing, in both free space [25] and fiber configurations [26]. In these experiments, the electric field transmitted by the FSL is measured by heterodyne mixing with a fraction of the seed laser on a photo-detector. In a second step, the backscattered electric field is measured by the same technique. Digital cross-correlation of both signals achieves pulse compression, and gives access to the reflectivity profile in amplitude and phase of the probe arm. The measurement rate can be as high as a few tens of MHz. However, the main drawback of the technique is the need for a detection bandwidth equal to that of the optical waveform. Since optical bandwidths at the

Optics EXPRESS

FSL output exceed the 10 GHz range (i.e. sub cm spatial resolution), this implies expensive fast detectors and analog-to-digital converters.

This limitation can be solved by performing the pulse compression in an analog all-optical way. For this, we have implemented a bidirectional FSL (Bi-FSL), which generates at the same time the probe and the reference waveform [27,28]. The latter is designed, so as to realize the pulse compression when the probe and the reference are recombined on a photo-detector. The Bi-FSL has already proven its interest in dual-comb interferometry [28] and in Lidar ranging [29], two features also based on pulse compression. In this work, we extend the capabilities of the Bi-FSL to distributed fiber sensing.

2.2. Pulse compression in the Bi-FSL

The Bi-FSL is a fiber loop, that contains an amplifier (EDFA), and a tunable optical bandpass filter (TBPF), both bi-directional (Fig. 1) [29]. It also incorporates a non-reciprocal section, made of two circulators and two acousto-optic frequency shifters. All fiber components are polarization-maintaining. The Bi-FSL is seeded in both ways by a single frequency CW laser at the telecom wavelength (frequency: f_0). The counter-propagating waves, labelled by 1 and 2, experience slightly different frequency shifts per round-trip (f_{s1} and f_{s2}, resp.), and slightly different travel times (τ_{c1} and τ_{c2}, resp.). The latter are controlled by two variable optical delay lines inserted next to the AOFS (not shown). Without loss of generality, we assume $f_{s2} - f_{s1} = \Delta f > 0$. Two output couplers enable to extract a fraction of the counter-propagating waves. In the spectral domain, the waveform 1 (resp. 2) consists of a frequency comb starting at f_0, and of spacing f_{s1} (resp. f_{s2}). The number of comb lines (N) is set by the TBPF. We consider that the shift frequencies are close enough, so that : $N\Delta f < f_{s1}/2$ ($\approx f_{s2}/2$), a condition usually encountered in dual-comb interferometry [30].

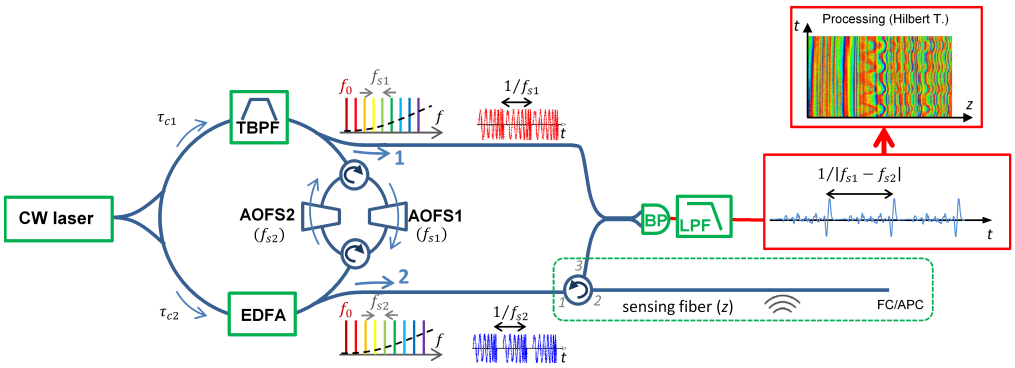

Fig. 1. Sketch of the experimental set-up. The Bi-FSL seeded with a CW laser (freq: f_0) generates two counter-propagating and mutually coherent optical frequency combs with slightly different frequency spacings (f_{s1} and f_{s2}), but identical quadratic spectral phases (see text). The corresponding waveforms in the time domain consist of trains of identical chirps, with slightly different repetition rates. After probing the sensing fiber, path #2 is recombined with the reference (path #1) on a balanced photo-detector (BP). After low-pass filtering (LPF), the signal trace (resulting from pulse compression) reproduces periodically (period: $1/\Delta f$) the real part of the reflectivity profile integrated over the fiber. Digital processing involving Hilbert transform enables to reconstruct the modulus and phase profiles along the sensing fiber.

Neglecting a linear component which only translates into a global temporal delay of the waveform, it can be shown that the comb spectral phases are quadratic (i.e. show a quadratic dependence with n, the line number) [22]. Assuming that all comb lines have the same power

Optics EXPRESS

(flat-top spectrum), the electric fields at the FSL outputs write [29]:

$$E_{1,2}(t) = E_0 e^{i2\pi f_0 t} \sum_{n=0}^{N-1} e^{i2\pi n f_{s1,2} t} e^{i\pi n^2 f_{s1,2} \tau_{c1,2}}. \quad (1)$$

As said, depending on the value of the product $f_{s1,2}\tau_{c1,2}$, the waveforms emitted by the FSL range from transform-limited pulses at repetition rate multiples of $f_{s1,2}$ when $f_{s1,2}\tau_{c1,2}$ takes a fractional value, to quasi continuous chirped waveforms when $f_{s1,2}\tau_{c1,2}$ slightly differs from integer values [19,22].

Assume now that waveform 2 (the probe) experiences a relative delay of 2τ with respect to waveform 1, considered as the reference. (The factor of 2 in the delay is due to the round-trip propagation time in a typical ranging experiment.) Recombining the waveforms on a balanced photo-detector provides an output signal equal to: $I(t) = E_1(t)E_2^*(t-2\tau) + C.C.$ (In the following, we omit the complex conjugate $C.C.$ in the expressions of the output signal.) One has:

$$I(t) = E_1(t)E_2^*(t-2\tau) = I_0 e^{i4\pi f_0 \tau} \sum_{n,m} e^{i2\pi(nf_{s1} - mf_{s2})t} e^{i4\pi m f_{s2}\tau} e^{i\pi n^2 (f_{s1}\tau_{c1} - f_{s2}\tau_{c2})} \quad (2)$$

where $I_0 = E_0 E_0^*$. Similarly to conventional dual-comb systems, a low-pass filter (cut-off frequency : $N\Delta f$) enables to filter out all beatnotes where $n \neq m$. In the following, we consider the case where the system is set such that the travel times τ_{c1} and τ_{c2} satisfy: $f_{s1}\tau_{c1} = f_{s2}\tau_{c2}$. In other words, the quadratic spectral phases of both combs are equal. Additionally, when the Bi-FSL emits chirped waveforms, the chirp rates are identical. Then, the output signal rewrites :

$$I(t) = I_0 e^{i4\pi f_0 \tau} \sum_n e^{-i2\pi n\Delta f t} e^{i4\pi n f_{s2}\tau} = I_0 e^{i4\pi f_0 \tau} J(t - 2\tau') \quad (3)$$

where we have defined $J(t) = \sum_n e^{i2\pi n\Delta f t}$ and $\tau' = \frac{f_{s2}}{\Delta f}\tau$. $J(t)$, which can be seen as the impulse response of the interrogator, is a periodic train of sharp pulses (period: $T = 1/\Delta f$), of duration $\simeq 1/(N\Delta f)$. These sharp pulses result from the pulse compression of the probe electric field $E_2(t)$ by the reference one $E_1(t)$. The time shift of the output signal τ' is proportional to the delay τ, showing the suitability of the set-up for time-domain ranging. The resolution, expressed in propagation time, is given by the pulse duration $(1/Nf_{s2})$: it is set by the bandwidth of the optical frequency combs. The ambiguity range (also expressed in propagation time) is $\tau_a = 1/f_{s2}$, which corresponds to the period of the optical pulse trains. Recall that in a typical reflectometry setup, a factor of $1/2$ should be considered in the resolution and in the ambiguity range, to take into account the round-trip from the source to the detector. Since the detection technique is intrinsically coherent, the phase provides meaningful information. The latter can be directly extracted by an I/Q analog demodulation [31], or by computing numerically in real time the Hilbert transform of the output signal [29]. This is the approach we have used here.

2.3. Application of the Bi-FSL to distributed sensing

Output signal of a distributed sensor based on Rayleigh scattering In the case of distributed sensing, the expression of the output signal should include contributions of scatterers distributed all along the sensing fiber. We consider that the latter extends from $z = 0$ to L. We assume that the round-trip propagation time in the sensing fiber (i.e. from $z = 0$ to L) is equal to the ambiguity range $\tau_a = 1/f_{s2}$, i.e.: $L = \frac{c}{2n_0 f_{s2}}$, where n_0 is the fiber refractive index at frequency f_0 (we neglect here the fiber dispersion). We introduce A_i the complex reflection coefficient of scatterer i, and τ_i the (one-way) propagation time from the sensing fiber input ($z = 0$) to the scatterer i.

Optics EXPRESS

Neglecting multiple scattering events, the electric field in the probe arm, after propagation, scattering and retro-propagation to $z = 0$, writes:

$$E_2(t) = E_0 \sum_i A_i \sum_{m=0}^{N-1} e^{i2\pi(f_0+mf_{s2})(t-2\tau_i)} e^{i\pi m^2 f_{s2}\tau_{c2}}. \quad (4)$$

The discrete distribution of scatterers can be approximated by a continuous complex reflectivity function $A(\tau)$. Then,

$$E_2(t) = E_0 \int_0^{\tau_a/2} A(\tau) \sum_{m=0}^{N-1} e^{i2\pi(f_0+mf_{s2})(t-2\tau)} e^{i\pi m^2 f_{s2}\tau_{c2}} d\tau. \quad (5)$$

Similarly to τ_i, the variable τ stands for the (one-way) propagation time from the fiber input ($z = 0$) to the scatterer. The recombination of the probe $E_2(t)$ with the reference $E_1(t)$ on a balanced photo-detector followed by low-pass filtering leads to:

$$I(t) = I_0 \int_0^{\tau_a/2} A^*(\tau) e^{i4\pi f_0\tau} \sum_n e^{-i2\pi n\Delta f t} e^{i4\pi n f_{s2}\tau} d\tau = I_0 \int_0^{\tau_a/2} A^*(\tau) e^{i4\pi f_0\tau} J\left(t - 2\frac{f_{s2}}{\Delta f}\tau\right) d\tau. \quad (6)$$

A change of variable gives:

$$I(t) \propto \int_0^{T/2} A'^*(\tau') J(t - 2\tau') d\tau' \quad (7)$$

where $A'(\tau') = A\left(\frac{\Delta f}{f_{s2}}\tau'\right) e^{-i4\pi f_0 \frac{\Delta f}{f_{s2}}\tau'} = A(\tau) e^{-i4\pi f_0\tau}$. Recall that $\frac{f_{s2}}{\Delta f}\tau_a = T$. Equation (7) shows that the architecture can be seen as a linear response system, where the output signal is the convolution product of the complex backscattering function of the fiber (multiplied by a linear phase factor), by J, the impulse response of the interrogator. The period of the output signal is T. In the limit where the impulse function of the interrogator J is approximated by a Dirac delta comb of period T, i.e. $J(t) = \sum_k \delta(t - kT)$, the output signal in the interval $0<t<T$ rewrites:

$$I(t) = I_0 A^*\left(\frac{\Delta f}{2f_{s2}}t\right) e^{i2\pi \frac{f_0\Delta f}{f_{s2}}t}. \quad (8)$$

In other words, the output signal consists of a scaled replica of the scattering function A multiplied by a phase term. The proportionality relation between z, the position along the fiber, and t, the measurement time, simply writes: $z = \frac{c\Delta f}{2n_0 f_{s2}}t$.

Monitoring of the refractive index profile along the fiber To give an example, we now suppose that a localized perturbation producing a phase jump of ϕ is applied in the sensing fiber at a location corresponding to a (one-way) propagation time in the sensing fiber equal to $\tau_0/2$. The additional time delay that corresponds to this phase jump is equal to: $\delta\tau = \phi/(2\pi f_0)$. Then,

$$I(t) \simeq I_0 \int_0^{\tau_0/2} A^*(\tau) e^{i4\pi f_0\tau} J\left(t - 2\frac{f_{s2}}{\Delta f}\tau\right) d\tau + I_0 e^{i4\pi f_0\delta\tau} \int_{\tau_0/2}^{\tau_a/2} A^*(\tau) e^{i4\pi f_0\tau} J\left(t - 2\frac{f_{s2}}{\Delta f}\tau\right) d\tau. \quad (9)$$

Consider a single period of the output signal ($0<t<T$). Equation (9) shows that in the interval $0<t<\tau_0'$ (with $\tau_0' = \frac{f_{s2}}{\Delta f}\tau_0$), the output signal is given by: $I(t) = I_0 A^*\left(\frac{\Delta f}{2f_{s2}}t\right) e^{i2\pi \frac{f_0\Delta f}{f_{s2}}t}$, and is identical to the static case where no phase jump is applied. However, for $\tau_0'<t<T$, $I(t) = I_0 e^{i4\pi f_0\delta\tau} A^*\left(\frac{\Delta f}{2f_{s2}}t\right) e^{i2\pi \frac{f_0\Delta f}{f_{s2}}t}$. In other words, it is simply phase-shifted by 2ϕ as compared to the static case. (Again, the factor of 2 results from the round-trip in the sensing fiber). This

Optics EXPRESS

illustrates a primary feature of the technique: the capability to perform a quantitative measurement of localized phase changes along the fiber. This property can be extended to the general case, where a distributed index variation $n(z) = n_0 + \epsilon(z)$ is imprinted to the sensing fiber. In this case, the output signal writes:

$$I(t) = I_0 \int_0^{\tau_a/2} A^*(\tau) e^{i4\pi f_0 \tau} e^{i4\pi \frac{f_0}{c} \int_0^{\frac{c\tau}{n_0}} \epsilon(z)dz} J\left(t - 2\frac{f_{s2}}{\Delta f}\tau\right) d\tau. \tag{10}$$

Again, Eq. (10) simplifies by approximating the impulse function of the interrogator J to a Dirac delta function on the interval $0<t<T$:

$$I(t) = I_0 A^*\left(\frac{\Delta f}{2f_{s2}}t\right) e^{i4\pi \frac{f_0 \Delta f}{f_{s2}} t} e^{i4\pi \frac{f_0}{c} \int_0^{\frac{c\Delta f}{2n_0 f_{s2}} t} \epsilon(z)dz}. \tag{11}$$

The output signals with -i.e. $I(t)$- and without -i.e. $I_{\text{ref}}(t)$- the applied index variation differ only by a phase factor:

$$I(t) = I_{\text{ref}}(t) \times e^{i4\pi \frac{f_0}{c} \int_0^{\frac{c\Delta f}{2n_0 f_{s2}} t} \epsilon(z)dz} \tag{12}$$

which shows the capability to perform quantitative measurements of the index variation along the sensing fiber. More precisely, the relative index variation $\epsilon(z)$ can be obtained by derivation of the phase of the output signal according to:

$$\epsilon(z) = \frac{1}{4\pi} \frac{c}{f_0} \frac{d\phi(z)}{dz} \tag{13}$$

where $\phi(z)$ is the relative phase accumulated over a round-trip in the sensing fiber from $z = 0$ to z. Since in our set-up, the accumulated phase is mapped in the temporal domain, $\epsilon(z)$ can be deduced from the temporal variation of the phase $\phi(t)$ of the output signal:

$$\epsilon(z) = n_0 \frac{f_{s2}}{2\pi f_0 \Delta f} \frac{d\phi(t)}{dt} = n_0 \frac{f_{s2}}{2\pi f_0 \Delta f} \frac{\delta\phi}{\delta t} \tag{14}$$

where $\delta\phi$ is the variation of the phase measured during a time step δt.

Finally, recall that the complex conjugate has been omitted in the expressions of the output signal $I(t)$. In practice, the signal measured by the detector is the real part of $I(t)$. As said, in our experiments, the extraction of the modulus and phase is processed numerically, by computing the Hilbert transform of the output signal.

3. Characterization of the interrogator

First, we characterize the output signal measured in a sensing fiber without external perturbation. The parameters of the FSL are the following: $f_{s1} = 80.000$ MHz, $f_{s2} = 80.020$ MHz. The frequency combs contain about $N = 200$ comb lines, a value measured by recombining directly $E_1(t)$ and $E_2(t)$ on the balanced photo-detector and performing the Fourier transform of the output signal [29]. The spectral bandwidth of the combs is 16 GHz (200×80 MHz), which leads to a coherence length of 1.9 cm in vacuum. Taking into account the refractive index of the fiber and the factor of two due to the round-trip propagation, the resolution in a fiber reflectometry configuration is 7 mm. The travel times τ_{c1} and τ_{c2} are adjusted by means of the variable delay lines so that: $f_{s1}\tau_{c1} = f_{s2}\tau_{c2} = 10.005$. In this condition, the Bi-FSL emits chirps (the product $f_{s1,2}\tau_{c1,2}$ is close to an integer value) [19], and it enables pulse compression (the chirp rates are identical). At the Bi-FSL outputs, both optical fields have the same power (−15 dBm). The probe field $E_2(t)$ is amplified in an EDFA (power at the EDFA output: 6.5 dBm), and sent to the input port of a circulator (port 1). The fiber in port 2 (60 cm long, corresponding to an optical

Optics EXPRESS

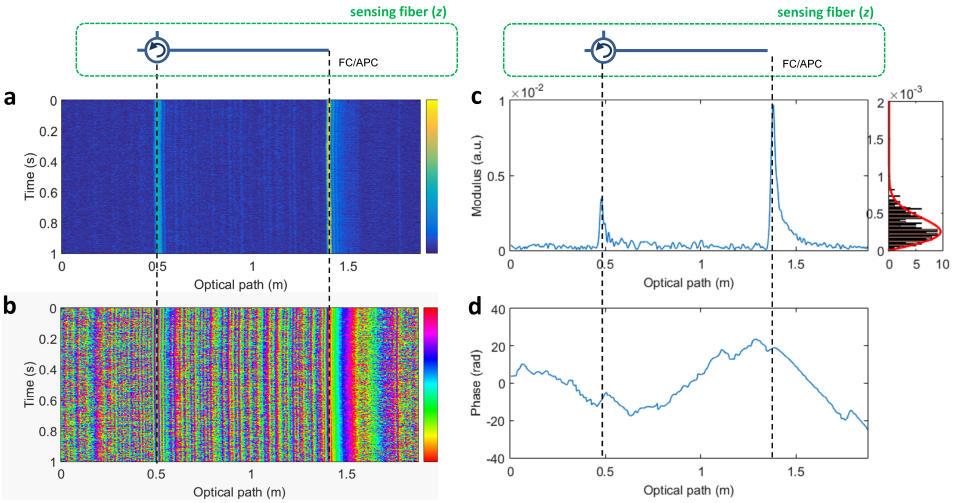

Fig. 2. Interrogation of the sensing fiber without external perturbation. The interrogation region (between 0.5 and 1.4 m optical path) is located between the circulator, and the FC/APC coupler. a,b: Waterfall plots of the modulus (a) and of the phase (b) of the output signal as a function of the position along the sensing fiber during 1 s. The colorbar next to the phase plot is in radians. c: Histogram of the values of the modulus in the region between 0.7 and 1.3 m averaged over 10 consecutive time traces. The red curve is a Rayleigh probability density function. d: Phase of the output signal along the sensing fiber.

path of 85 cm) is used as the sensing fiber. It is terminated by a FC/APC connector. In order to minimize the light backscattered from the end connector, the latter is plunged into water. The light backscattered from the sensing fiber (total power: −51 dBm) exits through port 3, where is is recombined with the reference field $E_1(t)$, and sent to a balanced photo-detector (75 MHz bandwidth). The output signal is filtered (cutt-off frequency: 4.5 MHz), recorded by a digitizer (10 MSa/s), and numerically processed on the fly. Computing the Hilbert transform enables to retrieve the modulus and the phase of the backscattered signal. The output signal consists of a periodic trace (period: $1/\Delta f = 50\ \mu$s). Each period can be displayed as a row of a matrix. This waterfall plot enables to visualize the temporal variations of the signal at a fixed position in the fiber as well as the spatial variations of the signal at a given time. In the following, the horizontal scale ("Optical path") corresponds to the distance along the fiber, multiplied by the refractive index of silica, i.e. 1.44.

In our experiments, the output traces contain two prominent peaks (Fig. 2). The first one corresponds to the reflection in the ferrule of the circulator. The second one is due to the FC/APC connector. The width of this peak determines the spatial resolution of the technique, a value close to 1 cm, in agreement with the 16 GHz-spectral bandwidth of the combs at the FSL output. The signal between theses two peaks corresponds to the signal due to Rayleigh scattering in the sensing fiber and, according to Eq. (8), maps the function $A(\tau)$. The modulus and the phase of $A(\tau)$ can be extracted from the output signal owing to a Hilbert transform. Because of the weakness of the return signal, the SNR of a single trace is close to unity. More precisely, the values of the modulus of the output signal in the interrogation zone (optical path comprised between 0.5 and 1.4 m) barely exceed the values outside this zone. To increase the SNR, consecutive traces can be averaged, prior to Hilbert transform. In Fig. 2(c). 10 consecutive traces have been averaged, which brings the return signal in the interrogation zone significantly above that outside the zone. Because of the random nature of the location of the scatterers in the fiber, the function A can be seen as a sum of random phasors in the complex plane, and its

Optics EXPRESS

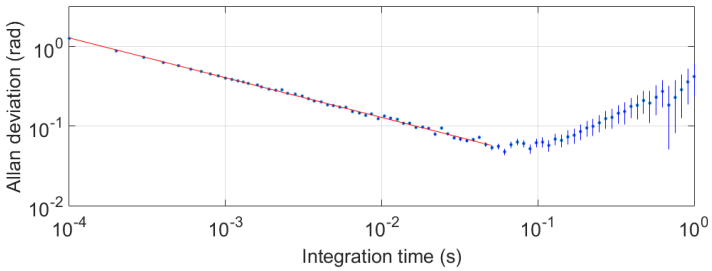

Fig. 3. The Allan deviation of the measurement of the local phase is plotted as a function of the integration time. The deviation decreases as the inverse square root of the integration time (red line). Beyond a few tens of ms, the deviation increases, due to slows drifts of the system (thermal fluctuations, mechanical constraints).

modulus is expected to follow a Rayleigh probability density function [32,33]. Recall that noise here has several contributions, including the ASE circulating in the Bi-FSL [34], the ASE of the amplifier before the sensing fiber, and the electronic noise of the detection chain.

In Fig. 3, we plot the Allan deviation of the phase measured at an arbitrary position in the interrogation zone. Up to an integration time close to 100 ms, the deviation decreases as the inverse of the square root of the integration time. Beyond this value, fluctuations with a larger time scale occur in the fiber (thermal and mechanical drifts), increasing the Allan deviation. Nevertheless, the architecture enables to measure the local phase of the Rayleigh scattering with a standard deviation of 1 rad in an integration time of 150 μs, and of 50 mrad in an integration time of 50 ms. Additionally, the sensitivity of the technique can be evaluated by: $S = \frac{\sigma_\phi}{\sqrt{BW}}$, where σ_ϕ is the standard deviation of the phase measurement, and BW is the measurement bandwidth. Taking $\sigma_\phi = 1.5$ rad and $BW = 4.5$ MHz leads to $S = 0.7$ mrad/$\sqrt{Hz}$.

4. Experimental results

In this section we report experimental results of distributed sensing.

4.1. Characterization of a phase modulator

In a first set of experiments, we prove the capability of the architecture to monitor in a quantitative manner the accumulated phase and the local index in the sensing fiber. First, we insert in the sensing fiber a phase modulator (PM, $V_\pi = 3.5$ V), in order to apply a controlled phase, i.e. a controlled refractive index variation. In this experiment, the output fiber of the circulator port 2 is 60 cm long. The end is connected to the PM, whose fiber terminations have been shortened down to 15 cm. Then, taking into account the length of the PM, the total length of the sensing fiber is 100 cm (i.e. 144 cm optical path).

First, a sine wave (5 Hz) is applied to the phase modulator. The amplitude is set between 0 and 4.2 V (Fig. 4(a)). The experimental output signals are acquired, processed (Hilbert transform), and the accumulated phase at the PM output is measured as a function of time. We extract the value of the amplitude of the phase variations, and plot it as a function of the amplitude of the applied voltage. The experimental results are displayed in Fig. 4. Figure 4(b) shows the linearity between the measured phase shift at the PM output with the PM voltage. As expected, the voltage corresponding to a phase shift of π is equal to 3.5 V.

We now show how the technique enables a quantitative and local measurement of the temporal variations of the refractive index along the fiber. For this aim, we apply a square wave signal to the PM (frequency: 5 Hz). First, the peak-to-peak amplitude of the applied voltage is set to $V_\pi/2$. The raw phase waterfall is displayed in Fig. 5(a). The phase variations are clearly visible

Optics EXPRESS

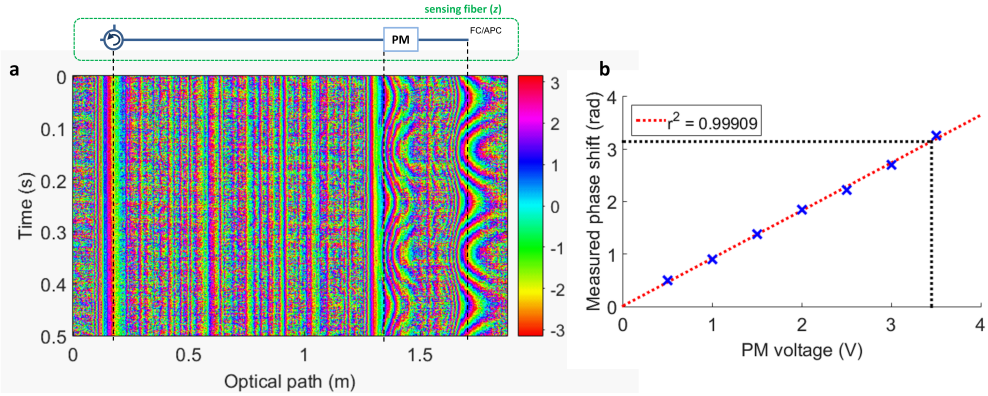

Fig. 4. Characterization of phase modulator (PM) in the sensing fiber. a: Typical phase profile along the fiber when the PM is driven with a 5 Hz frequency sine wave. b: variation of the phase shift measured after the PM with the voltage applied on the PM. The measured V_π is 3.5 V, in agreement with the value provided by the manufacturer.

for an optical path range between 1.3 and 1.8 meters, i.e. after the PM. To extract the refractive index variations, we proceed to the following steps. First, to increase the SNR, we perform an averaging over ten consecutive traces (duration of an individual trace: 50 μs = $1/\Delta f$). Then, the phase is unwrapped, and a linear component is removed from the phase profile. Next, a reference phase profile is extracted by averaging the phase profiles over 20 consecutive averaged traces. The reference phase profile is subtracted to all phase profiles. Finally, a numerical filter is applied to smooth the phase profiles, and a derivation is performed, following Eq. (13) and Eq. (14). Experimental results are shown in Fig. 5(b). The experiment is repeated for a peak-to-peak amplitude of the PM voltage equal to V_π (Fig. 5(b) and 5(d)). The waterfall plots in Fig. 5(b) and 5(d) evidence the capability of measuring the local refractive index. Figure 5(d) indicates a change of the refractive index inside the modulator of $\approx 1.9\,10^{-5}$. Integrating this value over the length of the active region of the modulator (4 cm in our case, i.e. 6 cm optical path) leads to a variation of the phase at the PM output of ≈ 3.1 radians, i.e. very close to π. This reveals the capability of the technique to monitor in real time the distributed variations of the refractive index with a resolution in the cm range.

4.2. *Time and space resolved monitoring of the refractive index in a fiber*

In a second set of experiments, we apply external mechanical perturbations on the fiber by tapping on it with a finger, and characterize the variations of the refractive index. First, we apply repeated tapping on the fiber, at a distance of 45 cm from the circulator (i.e. 63 cm optical path). In Fig. 6(a), we plot the raw phase profile. Repeated phase changes are clearly visible along the sensing fiber, starting from the position of the tapping. Following the procedure described above (averaging over 10 consecutive traces, unwrapping, subtracting the reference, filtering and derivation), the variation of the refractive index is extracted, and plotted in Fig. 6(b). As expected, these variations are localized at the position and at the time of the tapping. Next, we repeat the experiment by applying at the same location, a very brief tapping ($\approx$ 10 ms-duration). The results displayed in Fig. 6(c) and 6(d) show that the tapping can be localized spatially and temporally, at the cm and ms scale respectively.

Optics EXPRESS

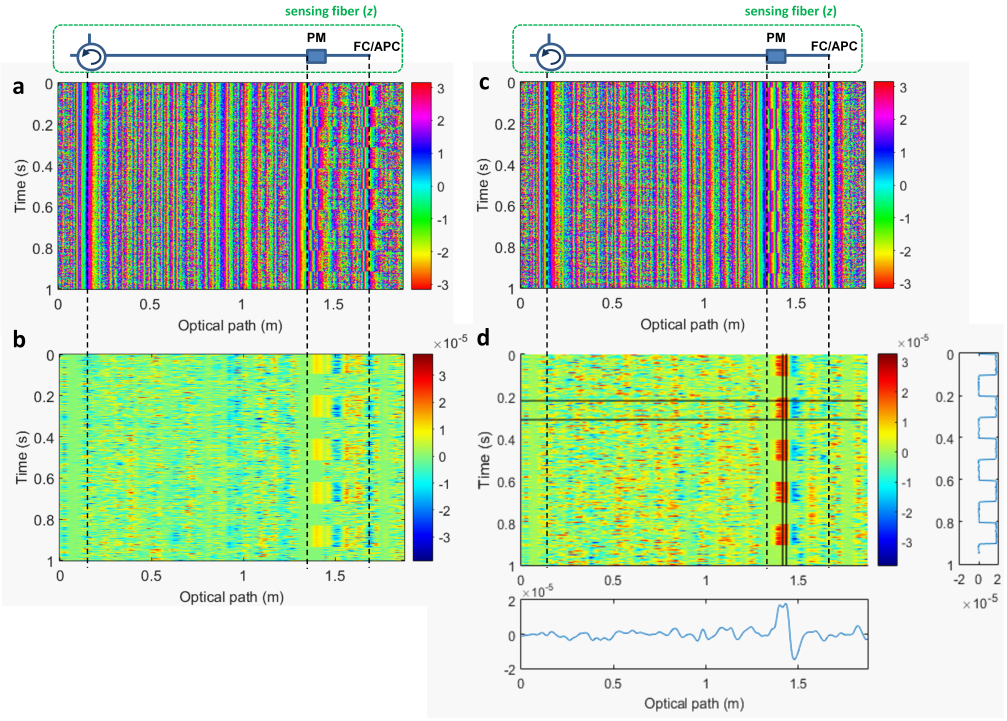

Fig. 5. a: Phase profile along the sensing fiber when a square wave signal (frequency: 5 Hz, peak-to peak amplitude: $V_\pi/2$) is applied to the PM. Due to the round-trip in the sensing fiber, the phase modulation produces phase jumps of π between the PM and the end of the sensing fiber (i.e. for an optical path between 1.35 and 1.75 m). The color bar next to the phase plot is in radians. b: Variation of the refractive index along the fiber. An index relative variation of $\approx 1.0 \times 10^{-5}$ is measured over a 6 cm-long optical path region that corresponds to the active area of the PM. c: The amplitude of the voltage applied to the PM is now V_π. Due to the round-trip, the modulation of the accumulated phase vanishes between the PM and the end of the sensing fiber. d: The index variation measured in the active region of the PM is $\approx 1.9 \times 10^{-5}$, i.e. close to twice to that of a and b. The two insets show the profiles of the index variations along the vertical and the horizontal stripes.

Optics EXPRESS

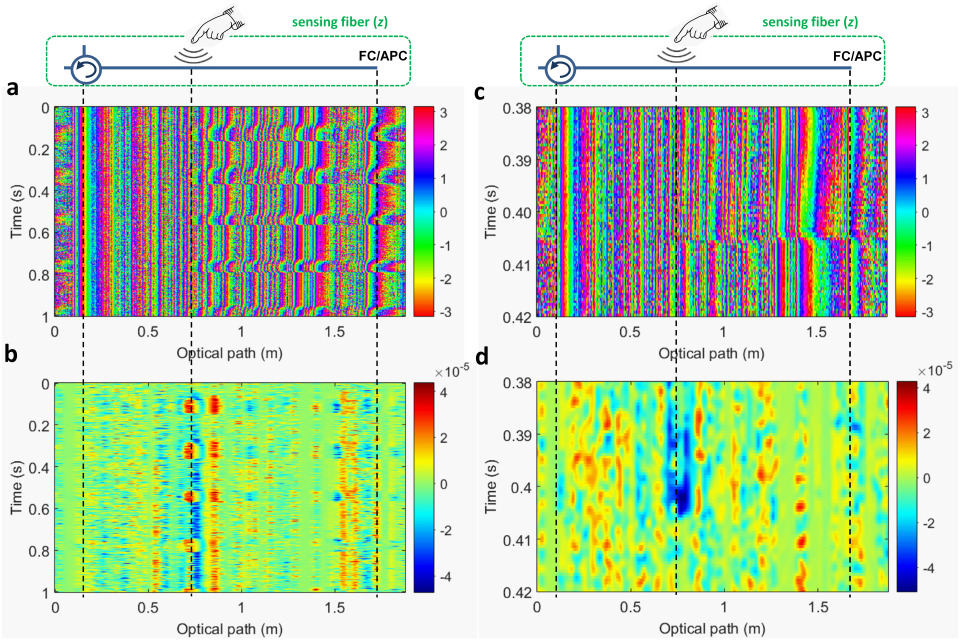

Fig. 6. a: Phase profile along the sensing fiber when repeated tapping is applied on the fiber. b: Reconstruction of the refractive index changes (see text). c: Phase profile along the sensing fiber submitted to a single and short tapping (≈ 10 ms). d: Reconstruction of the refractive index changes (see text).

4.3. Vibration analysis

In a last set of experiments, we perform frequency analysis of vibrations. First we place a rotating fan in contact with the sensing fiber, at a distance of 25 cm from the circulator. The recorded reflectivity and phase are plotted in Fig. 7(a) and 7b respectively. The signature of the vibration in the phase is clearly apparent (Fig. 7(b)). We perform a frequency analysis of the phase variations by computing the Fourier transform of the phase variations along all columns of the waterfall plot. The results are displayed on Fig. 7(c). They show that a complex acoustic signature can be measured beyond the position of the fan. Spectral components at multiples of 25 Hz are especially noticeable. Then, we use the same technique to localize different vibration sources distributed along the sensing fiber. Three loudspeakers are placed in contact with the sensing fiber at specific positions, and supplied with different tones (120, 440, and 1000 Hz). The module and phase waterfalls are plotted in Fig. 7(d) and 7e respectively. Computing the Fourier transform of the local phase leads to the spectrogram in Fig. 7(f). Again, the individual frequency components appear at the position of the corresponding loudspeaker. Notice however that the highest frequency (1000 Hz) seems to be detectable before the position of the corresponding speaker. This effect could be due to transmission of acoustic vibrations along the fiber.

Optics EXPRESS

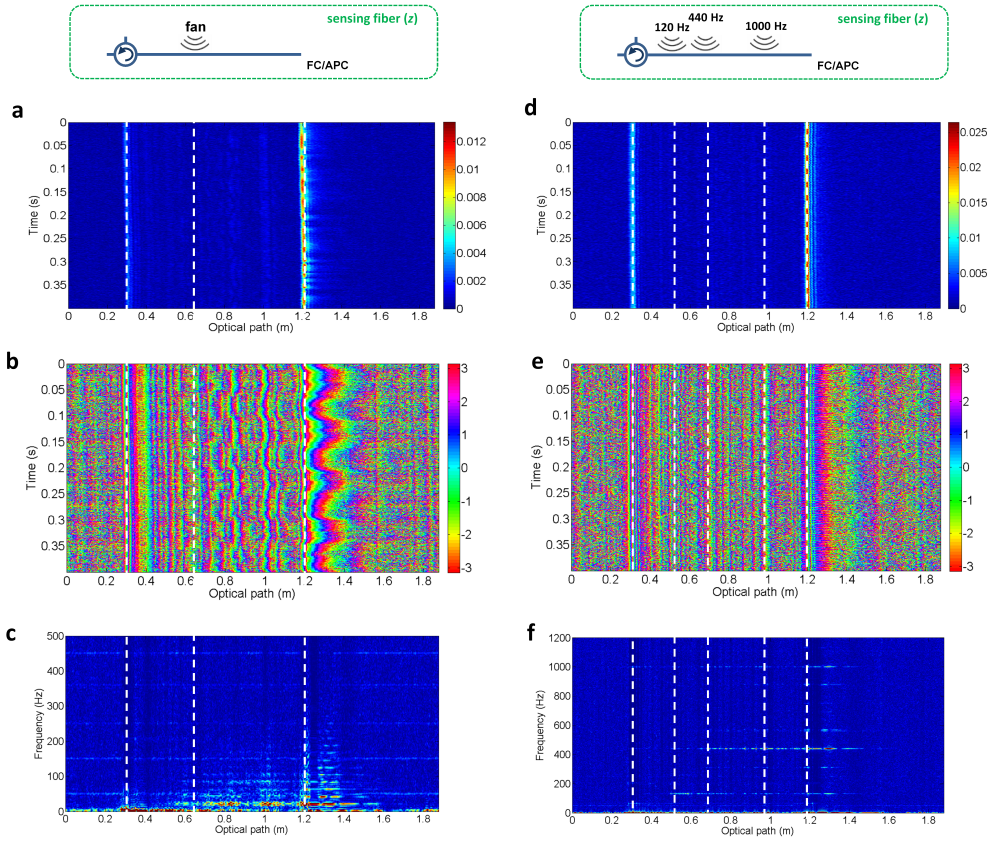

Fig. 7. Spectral analysis of vibrating sources. Left: a fan is placed in contact with the sensing fiber at 25 cm from the circulator (i.e. 36 cm optical path). a: Modulus of the reflectivity profile, b: Phase, c: Spectrogram (power spectrum as a function of the position along the fiber). d, e, f: Same experiment with three loud speakers at different frequencies placed along the fiber (see text).

5. Conclusion

We have reported a new fiber distributed acoustic sensing interrogator based on Rayleigh backscattering, enabling to monitor the accumulated phase and the refractive index with both sub-cm range resolution and tens of kHz acquisition rate. The system extends the capabilities of fiber sensing, and opens new perspectives, such as the distributed monitoring of fast and localized phenomena with a high resolution, including transient events. The architecture reported here is optimal in many aspects. First, the technique is coherent, which implies the capability of long range and of phase-sensitive measurements. The resolution is set by the spectral bandwidth of the optical waveforms rather than their duration, a property enabled by a pulse compression effect. To avoid the need for a fast detection, the latter is done in an all-optical fashion. Additionally, the optical waveforms used are quasi continuous, which renders them easy to amplify and delays the emergence of detrimental non-linear effects. Finally, the required hardware is strikingly simple: a single single-frequency laser, commercial telecom components, and a slow detection chain (10 MSa/s).

Regarding the performance of the technique, recall that the spatial resolution is set by the coherence length of the optical waveforms. In other words, the resolution could be improved by

Optics EXPRESS

increasing the spectral bandwidth of the combs generated in the Bi-FSL. However, increasing the number of lines beyond a few hundreds is challenging, mainly because of the growing role played by the ASE when the number of round-trips in the FSL increases, resulting in a decrease of the SNR [34,35]. Another possibility is to increase the combs free spectral range, e.g. by using electro-optic frequency shifters. But again a trade-off should be found between the resolution, the SNR and the ambiguity range. Interestingly, the product of the resolution (expressed in time) by the spectral bandwidth of the comb is equal to N, the number of frequency components in the combs. The temporal resolution of the technique is directly set by the acquisition rate, i.e. by Δf. In our system, it is currently equal to 20 kHz. The maximum acquisition rate in dual-comb systems, is equal to $f_{s2}/(2N)$. Considering $N = 200$ results in a maximum acquisition rate of 200 kHz, i.e. a temporal resolution of 5 μs. This could be attainable by using a faster acquisition time (100 MSa/s) and optimizing the processing to maintain real-time capability. Regarding the ambiguity range, it is determined by the comb spacing. In our case, with a spacing of 80 MHz, taking into account the roundtrip propagation and the fiber index, the ambiguity range in a fiber reflectivity configuration is 1.4 m. Therefore our technique is especially adapted to acoustics and vibrations at the meter scale, including for instance aero- and hydrodynamics.

Finally, it must be emphasized that we have demonstrated the capability of the interrogator is a worst case scenario. The sensing fiber is commercial single-mode PM fiber, with a typical Rayleigh reflectivity of the order of −100 dB/mm [10]. This means that for a 1 meter-long sensing fiber, the power of the signal of interest is reduced by - 70 dB as compared to the optical power transmitted in the fiber. Still, despite this drastic effect, the interrogator is able to measure the distributed backscattered signal with a SNR close to unity within a 50 μs interrogation time. Therefore, there are still clear prospects for improving the technique by increasing the reflectivity of the fiber. This could be done by doping the fiber with impurities so as to increase the Rayleigh scattering, or by imprinting specially-designed index modulation profiles (i.e. Bragg gratings) in the sensing fiber core [36].

Funding. Centre National de la Recherche Scientifique (Prématuration 2021); Agence Nationale de la Recherche (CE42- AAPG 2021).

Acknowledgments. We acknowledge support from the Agence Nationale de la Recherche ("COCOA" project, grant CE42- AAPG 2021), and from the Centre National de la Recherche Scientifique ("Photonic ASP" project, grant Prématuration 2021, CNRS). We thank Adélie Wagner and Adeline Dekooninck (Arcale Company), for the digital interface of the system.

Disclosures. The authors declare no conflicts of interest.

Data availability. Data underlying the results presented in this paper may be obtained from the authors upon request.

References

1. Y. Wang, J. Gong, D. Y. Wang, B. Dong, W. Bi, and A. Wang, "A Quasi-Distributed Sensing Network With Time-Division-Multiplexed Fiber Bragg Gratings," IEEE Photonics Technol. Lett. **23**(2), 70–72 (2011).
2. X. W. Ye, Y. H. Su, and J. P. Han, "Structural Health Monitoring of Civil Infrastructure Using Optical Fiber Sensing Technology: A Comprehensive Review," Scientific World J. **2014**, 1–11 (2014).
3. X. Lu, P. J. Thomas, and J. O. Hellevang, "A Review of Methods for Fibre-Optic Distributed Chemical Sensing," Sensors **19**(13), 2876 (2019).
4. M. R. Fernandez-Ruiz, M. A. Soto, E. F. Williams, S. Martin-Lopez, Z. Zhan, M. Gonzalez-Herraez, and H. F. Martins, "Distributed acoustic sensing for seismic activity monitoring," APL Photonics **5**(3), 030901 (2020).
5. X. Bao and L. Chen, "Recent progress in distributed fiber optic sensors," Sensors **12**(7), 8601–8639 (2012).
6. X. Bao and Y. Wang, "Recent advancements in Rayleigh scattering-based distributed fiber sensors," Adv. Devices Instrument. **2021**, 1–17 (2021).
7. J. Pastor-Graells, H. F. Martins, A. Garcia-Ruiz, S. Martin-Lopez, and M. Gonzalez-Herraez, "Single-shot distributed temperature and strain tracking using direct detection phase-sensitive OTDR with chirped pulses," Opt. Express **24**(12), 13121–13133 (2016).
8. Y. Lu, T. Zhu, L. Chen, and X. Bao, "Distributed Vibration Sensor Based on Coherent Detection of Phase-OTDR," J. Lightwave Technol. **28**(22), 3243–3249 (2010).
9. Y. Muanenda, "Recent Advances in Distributed Acoustic Sensing Based on Phase-Sensitive Optical Time Domain Reflectometry," J. Sensors **2018**, 1–16 (2018).

Optics EXPRESS

10. Y. Rao, Z. Wang, H. Wu, Z. Ran, and B. Han, "Recent Advances in Phase-Sensitive Optical Time Domain Reflectometry (Φ-OTDR)," Photonic Sens. **11**(1), 1–30 (2021).
11. D. Uttam and B. Culshaw, "Precision time domain reflectometry in optical fiber systems using a frequency modulated continuous wave ranging technique," J. Lightwave Technol. **3**(5), 971–977 (1985).
12. H. Li, Q. Liu, D. Chen, Y. Deng, and Z. He, "High-spatial-resolution fiber-optic distributed acoustic sensor based on Φ-OFDR with enhanced crosstalk suppression," Opt. Lett. **45**(2), 563–566 (2020).
13. S. T. Kreger, A. K. Sang, N. Garg, and J. Michel, "High resolution, high sensitivity, dynamic distributed structural monitoring using optical frequency domain reflectometry," Proc. SPIE **8722**, 87220D (2013).
14. N. Levanon and E. Mozeson, *Radar signals*, John Wiley & Sons, 2004.
15. R. E. Ziemer and W. H. Tranter, *Principles of Communications*, John Wiley & Sons, 1988.
16. M. Wu, X. Fan, Q. Liu, and Z. He, "Quasi-distributed fiber-optic acoustic sensing system based on pulse compression technique and phase-noise compensation," Opt. Lett. **44**(24), 5969–5972 (2019).
17. H. Guillet de Chatellus, L. Romero Cortés, and J. Azaña, "Optical real-time Fourier transformation with kilohertz resolutions," Optica **3**(1), 1–8 (2016).
18. C. Schnébelin and H. Guillet de Chatellus, "Agile photonic fractional Fourier transformation of optical and RF signals," Optica **4**(8), 907–910 (2017).
19. H. Guillet de Chatellus, L. Romero Cortés, M. Burla, and J. Azaña, "Reconfigurable photonic generation of broadband chirped waveforms using a single CW laser and low-frequency electronics," Nat. Commun. **9**(1), 2438 (2018).
20. C. Schnébelin, J. Azaña, and H. Guillet de Chatellus, "Programmable broadband optical field spectral shaping with megahertz resolution using a simple frequency shifting loop," Nat. Commun. **10**(1), 4654 (2019).
21. G. Bourdarot, J.-P. Berger, and H. Guillet de Chatellus, "Multi-delay photonic correlator for wideband RF signal processing," Optica **9**(4), 325–334 (2022).
22. H. Guillet de Chatellus, E. Lacot, W. Glastre, O. Jacquin, and O. Hugon, "Theory of Talbot lasers," Phys. Rev. A **88**(3), 033828 (2013).
23. H. Guillet de Chatellus, L. Romero Cortés, and J. Azaña, "Arbitrary energy-preserving control of the line spacing of an optical frequency comb over six orders of magnitude through self-imaging," Opt. Express **26**(16), 21069–21085 (2018).
24. J. Clement, H. Guillet de Chatellus, and C. R. Fernández-Pousa, "Far-field Talbot waveforms generated by acousto-optic frequency shifting loops," Opt. Express **28**(9), 12977–12997 (2020).
25. J. Clement, C. Schnébelin, H. Guillet de Chatellus, and C. R. Fernández-Pousa, "Laser ranging using coherent pulse compression with frequency shifting loops," Opt. Express **27**(9), 12000–12010 (2019).
26. V. Billault, G. Arpison, V. Crozatier, V. Kemlin, L. Morvan, D. Dolfi, and H. Guillet de Chatellus, "Coherent Optical Fiber Sensing Based on a Frequency Shifting Loop," J. Lightwave Technol. **39**(12), 4118–4123 (2021).
27. V. Duran, C. Schnébelin, and H. Guillet de Chatellus, "Coherent multi-heterodyne spectroscopy using acousto-optic frequency combs," Opt. Express **26**(11), 13800–13809 (2018).
28. V. Duran, L. Djevarhidjian, and H. Guillet de Chatellus, "Bidirectional frequency-shifting loop for dual-comb spectroscopy," Opt. Lett. **44**(15), 3789–3792 (2019).
29. V. Billault, V. Duran, C. R. Fernández-Pousa, V. Crozatier, D. Dolfi, and H. Guillet de Chatellus, "All-optical coherent pulse compression for dynamic laser ranging using an acousto-optic dual comb," Opt. Express **29**(14), 21369–21385 (2021).
30. I. Coddington, N. Newbury, and W. Swann, "Dual-comb spectroscopy," Optica **3**(4), 414–426 (2016).
31. Z. Wang, L. Zhang, S. Wang, N. Xue, F. Peng, M. Fan, W. Sun, X. Qian, J. Rao, and Y. Rao, "Coherent Φ-OTDR based on I/Q demodulation and homodyne detection," Opt. Express **24**(2), 853–858 (2016).
32. J. W. Goodman, *Statistical Optics*, John Wiley & Sons, 2015.
33. H. Gabai and A. Eyal, "On the sensitivity of distributed acoustic sensing," Opt. Lett. **41**(24), 5648–5651 (2016).
34. C. Fernández-Pousa and H. Guillet de Chatellus, "Fundamental SNR limits imposed by ASE in frequency-shifting loops," J. Lightwave Technol. **40**(20), 6831–6844 (2022).
35. N. Kanagaraj, L. Djevarhidjian, V. Duran, C. Schnébelin, and H. Guillet de Chatellus, "Optimization of acousto-optic optical frequency combs," Opt. Express **27**(10), 14842–14852 (2019).
36. Y. Wang, P. Lu, S. Mihailov, L. Chen, and X. Bao, "Distributed time delay sensing in a random fiber grating array based on chirped pulse Φ-OTDR," Opt. Lett. **45**(13), 3423–3426 (2020).